Journal of
Materials Chemistry A

Materials for energy and sustainability

Accepted Manuscript

This article can be cited before page numbers have been issued, to do this please use: J. Xie, S. Sankarasubramanian, J. G. Catalano and V. Ramani, *J. Mater. Chem. A*, 2026, DOI: 10.1039/D6TA01059H.

ROYAL SOCIETY OF CHEMISTRY

rsc.li/materials-a

View Article Online
DOI: 10.1039/D6TA01059H

Title page

Decoupling Redox Actives Solubility and Energy Density in Redox Flow Batteries Using Supersaturated, Phase-change Electrolytes

Jing Xie[a], Shrihari Sankarasubramanian[b, c], Jeffrey G. Catalano[d], Vijay Ramani*[a]

[a]Department of Energy, Environmental & Chemical Engineering, Washington University in St. Louis, St. Louis, MO 63130; [b]Department of Biomedical Engineering and Chemical Engineering, University of Texas at San Antonio, San Antonio, TX 78429; [c]Department of Mechanical, Aerospace and Industrial Engineering, University of Texas at San Antonio, San Antonio, TX 78429; [d]Department of Earth and Planetary Sciences, Washington University in St. Louis, St. Louis, MO 63130.

*Corresponding author: Vijay Ramani; 1 Brookings Drive, South Brookings Hall, Room 135, St. Louis, MO 63130; 314-935-7924; ramani@wustl.edu

Keywords: redox flow battery, hydrolysis, complexation, supersaturation

View Article Online
DOI: 10.1039/D6TA01059H

Abstract

Redox flow batteries (RFBs), with their characteristic decoupling of power density and energy capacity, are scalable energy storage systems that can help smooth out the intermittency of solar and wind power on the electric grid. Amongst the many different redox couples considered in RFBs, the cerium (Ce) redox couple, Ce(IV)/Ce(III), is particularly attractive due to its high standard potential (1.61 V vs. standard hydrogen electrode, SHE) and the relative abundance of Ce in the Earth crust (as abundant as lead). Ce-based RFBs such as the Zn-Ce system have been scaled-up and commercialized but meeting ever lower energy storage cost targets (<\$50 kWh^{-1}) requires significantly higher Ce electrolyte energy density. Herein, in a departure from previous studies which utilize acid-supported Ce electrolyte solutions (e.g., sulfuric acid), we have developed a new Ce electrolyte with ammonium sulfate (AS) working as the supporting electrolyte. The solubility of Ce(IV) was enhanced to 1.23 M by optimizing the ratio between Ce salt and AS. This ~40% increase in energy density was found to be a function of the solution chemistry with complementary effects of Ce(IV) hydrolysis with water and complexation with anions. This cost-effective Ce electrolyte was paired with the titanium (Ti) redox couple to demonstrate a high energy density, low-cost Ce-based RFB.

View Article Online
DOI: 10.1039/D6TA01059H

Introduction

Redox flow batteries (RFBs) have attracted significant attention due to their ability to decouple energy capacity from power output, making them ideal for large-scale energy storage systems[1]. While all-vanadium RFBs remain being studied and applied most widely, the high cost of raw material and relatively low output potential drive forward the research on other redox couples[2,3]. In the meantime, the development of aqueous inorganic RFBs is usually limited by the poor solubility of active species. As the most abundant and inexpensive rare earth element[4], cerium (Ce) has a broad range of applications such as automotive catalysts[5], wastewater treatment[6], alloys synthesis[7], and therapeutic agents[8]. Ce redox couple, Ce(IV)/Ce(III), has been utilized in electrochemical energy storage due to the high redox potential[9]. More specifically, Ce redox couple has been successfully incorporated into aqueous RFBs working as the positive side[10] and has been coupled with Zn, Pb, H_2, V, and Ti to yield a variety of RFBs[11]. The Zn-Ce RFB was even commercialized by Plurion before having to shut down due to the 2008 economic crisis. To our best knowledge, previous studies were dissolving Ce species into traditional acidic supporting electrolyte to enhance the stability and kinetics with the Ce solubility limited to (at best) 0.9M[12,13]. The Ce solubility in sulfuric acid (H_2SO_4) has been shown to decrease as the acid concentration increases, which is usually explained by "common ion effect"[14], while an inverse relationship between Ce(III) and Ce(IV) solubility could be seen in methanesulfonic acid (CH_3SO_3H)[15]. Due to the limitation of Ce solubility in acidic electrolyte, the concentration of active species in aqueous RFBs using Ce redox couple is usually below 1 M. Some reports exist of cerium redox in non-aqueous electrolytes like acetonitrile but the very low solubility (0.05M in this case[16]) makes these systems far from practical.

View Article Online
DOI: 10.1039/D6TA01059H

The study of solubility enhancement in aqueous inorganic RFBs is much more scarce compared to studies on organic actives[17], and most of the existing research is focusing on vanadium (V) RFBs[18]. The group of Prof. Skyllas-Kazacos has conducted a comprehensive study on the effect of different additives on supersaturated V electrolytes. They first proposed the idea of using "stabilizing agents" that do not promote V solubility but postpones precipitation by adsorbing to the nucleation sites to inhibit crystal growth[19]. According to their research, ammonium ion (NH_4^+) and phosphate ion (PO_4^{3-}) were shown to work best as precipitation inhibitors[20]. Unlike this study, the amount of effective additives in their studies was very low (e.g., 1 to 5 wt.%), which makes complexing an unlikely mechanism because it requires a comparable concentration between metal ions and complexing agents.

Building on our success developing the titanium (Ti)-Ce RFBs utilizing methanesulfonic acid as the supporting electrolyte and aiming to break through the existing Ce solubility limitation, we screened a series of non-acidic supporting electrolytes and a solution of ammonium sulfate (AS) was found to enable Ce(IV) solubility as high as 1.23 M. Unlike prior studies where a trace amount of additive added into conventional acidic electrolytes, AS is the only component of the electrolyte here apart from the dissolved Ce salt. Due to the high charge-to-radius ratio of Ce(IV), it easily hydrolyses with water when the solution pH is relatively high [21]. The near-neutral environment of AS solution favors for Ce(IV) hydrolysis and the release of protons, reducing pH. The resultant low-pH environment drives protonation of the Ce counterion sulfate (SO_4^{2-}) to form bisulfate (HSO_4^-), and the complexation between Ce(IV) and HSO_4^- tends to form a stable structure where the ratio of Ce(IV) to HSO_4^- is 1:3[22]. The synergistic effect of Ce(IV) hydrolysis, the resultant pH reduction and formation of bisulfate anions enabling favorable complexation serves as the foundation of our supersaturated electrolyte. This new Ce(IV) electrolyte was paired with the same

View Article Online
DOI: 10.1039/D6TA01059H

concentration of Ti in AS leading to a new type of RFB. Upon cycling, the Ce(III) ion exhibited much lower solubility compared to Ce(IV) and precipitated out of solution. But we were able to circulate the resultant slurry through the RFB and convert the Ce(III) back to dissolved Ce(IV). This phase change cycling was carried out for 20 cycles with no irreversible capacity fade and an energy efficiency (EE) higher than 70% at 50 mA cm^{-2} operating current density. Thus, we demonstrated a new Ce-based, slurry aqueous inorganic RFB with a theoretical energy density of 33 Ah L^{-1}.

Materials and Methods

Chemicals. $Ce(SO_4)_2 \cdot xH_2O$ (Alfa Aesar, 98%), $TiOSO_4$ (Sigma-Aldrich, 34%), and $VOSO_4$ (Sigma-Aldrich) were used as raw Ce(IV), Ti(IV), and V(IV) materials, respectively. H_2SO_4 (Sigma-Aldrich, 99%) and CH_3SO_3H (Sigma-Aldrich, 99%) were used as supporting electrolytes. The original Ce(IV), Ti(IV), and V(IV) solutions were prepared by dissolving the required amount of AS into deionized water first, then adding the corresponding amount of metal salt into the AS solution. A stirring bar was used to speed up the dissolution.

Characterization Methods. Ce L_{III}-edge X-ray absorption near-edge structure (XANES) spectra were measured using an EasyXAFS 300+ X-ray spectrometer[23]. The second harmonic of a spherically-bent Ge (211) crystal was used to select the incident beam energy, which was detected using a silicon drift detector. $Ce(SO_4)_2$ dissolved into AS solution was injected into a sample cell consisting of a 0.25 mm thick PTFE ring shim (25.4 mm outer diameter, 15.9 mm inner diameter) sealed on both sides with Kapton tape. CeO_2 and $Ce_2(SO_4)_3$ were ground in a mortar and pestle, spread as a uniform layer on cellulose tape, and then stacked in six layers for measurement to

View Article Online
DOI: 10.1039/D6TA01059H

optimized absorbance. Data were collected in transmission with the energy calibrated using a Cr metal foil, with the first in inflection point of the Cr K-edge set to 5989 eV. The spectrum of $Ce(SO_4)_2$ was obtained from the XAS Database at the Canadian Light Source (http://xasdb.lightsource.ca, sample ID: id12345). Data were calibrated and normalized in the Athena[24] interface to IFEFFIT[25]. Raman spectroscopy was performed using a Renishaw inVia confocal Raman spectrometer equipped with a 514 nm laser excitation source. The laser power at the sample surface was set to 2 mW, and spectra were collected by focusing the laser beam on the surface plasmon-coupled emission (SPCE) working electrode using a 50x objective lens with a numerical aperture of 0.9 and an exposure time of 30 s. Ultraviolet-visible spectroscopy (UV-Vis) was conducted using a Varian Cary 50Bio. The absorption spectra between 190 to 1100 nm with a scan rate of 600 nm min^{-1} was collected. A quartz cuvette with a path length of 10 mm was used, and the supporting electrolyte solution without Ce(IV) was used to do the baseline correction before running each sample.

Electrochemical Measurements. Cyclic voltammetry (CV) was conducted with a WaveNowXV Potentiostat Bundles (PINE Research). A three-electrode setup was used for the measurements: carbon paper (CP, AvCarb MGL 190, Fuel Cell Store) or carbon felt (CF, GFA 6, SGL Group) with 1 cm^2 surface area as the working electrode, Ag/AgCl as the reference electrode, and platinum wire as the counter electrode. The potential window of CV was 0 to 2 V vs. Ag/AgCl, and different scan rates (e.g., 2.5, 5, 7.5, and 10 mV s^{-1}) were selected for further calculation. The results were analyzed by Nicholson-Shain (N-S) equation and Klinger-Kochi (K-K) equation to obtain diffusion coefficient (D_0) and standard reaction rate constant (k_0)[26-28]. More details for the calculation process are shown in Results and Discussion.

View Article Online
DOI: 10.1039/D6TA01059H

Redox Flow Battery Tests. All tests were conducted with an 857 Redox Flow Cell Test System (Scribner). CF with a 6 mm thickness was cut to 5x5 cm leading to a 25 cm^2 surface area. Raw and heat treated (500 °C, 8 h, air atmosphere) CF was used as positive (Ce) and negative (Ti) side electrode, respectively. The separator was a quaternized cardo-poly(ether ketone)-based anion exchange membrane functionalized with trimethylamine (QPEK-C-TMA AEM) developed by our group and the synthesis details were listed in previous studies[29]. A serpentine type with enlarged inlet and outlet flow field was used as shown in SI Appendix, Fig. S1. A total of 50 mL electrolyte was used in each side. Since the original Ce(IV) and Ti(IV) electrolytes were in fully charged and discharged state, respectively, a V-Ti RFB was assembled by pairing V(IV) and Ti(IV) electrolytes and a single, full charge was operated at 50 mA cm^{-2} until the cell reached cut-off potential (2 V) to obtain a fully charged Ti electrolyte, which contains mostly Ti(III). Next, this Ti electrolyte was paired with the Ce(IV) electrolyte for the cycling test in the sequence of discharge followed by charge-discharge cycle. More details about the electrolyte composition and test protocol are in SI Appendix.

Results and Discussion

Determination of Ce(IV) Electrolyte Composition. Solutions of different chemicals which contain NH_4^+, PO_4^{3-}, or $-NH_2$ were screened for their effects on $Ce(SO_4)_2$ solubility as shown in Table 1. The AS solution was the only candidate which had a positive effect on Ce(IV) solubility, with the solubility of Ce(IV) in other solutions being even lower than that in pure water. It was apparent that both NH_4^+ and SO_4^{2-} are playing a role in promoting Ce(IV) solubility, as the substitution of either would disable the effect (e.g., both Na_2SO_4 and NH_4Cl solutions resulting in

View Article Online
DOI: 10.1039/D6TA01059H

poor Ce(IV) solubility). Optimizing the $Ce(SO_4)_2$ and AS system, the ratio of NH_4 to SO_4 was varied and found to have a significant impact on Ce(IV) solubility as shown in Table 2. Note that we use NH_4 and SO_4 instead of NH_4^+ and SO_4^{2-} to denote all different species of ammonium (e.g., NH_3 and NH_4^+) and sulfate (e.g., SO_4^{2-} and HSO_4^-) in solution. The optimum ratio of NH_4 to SO_4 was determined to be 0.6 and this resulted in the highest observed Ce(IV) solubility of 1.23 M. Moreover, it is noteworthy that when the ratio of NH_4 to SO_4 was fixed (i.e., at 0.6:1), the Ce(IV) solution remained stable only when Ce(IV) content reached a relatively high level (Solutions 1 and 4, Solutions 5 to 8 Table 2). The mechanism of this phenomenon is further discussed.

Table 1 Effects of different supporting electrolytes on $Ce(SO_4)_2$ solubility

Additive	Effect	Ce(IV) conc. (M)
$(NH_4)_2SO_4$	+	1.23
H_2SO_4	-	0.5
H_3PO_4	-	-
Na_2SO_4	-	-
CF_3SO_3H	-	-
$Ce(NH_4)_4(SO_4)_4$	-	0.1
NH_4Cl	-	-
CH_3COONH_4	-	-
NH_4SCN	-	-
$(NH_4)_2S_2O_8$	-	-
$NH_4SO_3NH_2$	-	-

* The "-" sign on Ce(IV) concentration column indicates that for the given type of supporting electrolyte, the lowest amount of $Ce(SO_4)_2$ in the dissolution experiment was not able to fully dissolve.

Table 2 Effects of the ratio between ammonium and sulfate on Ce(IV) electrolytes

Solution #	Ratio of NH_4 to SO_4	Nominal* Ce(IV) conc. (M)	Condition
1	0.6 : 1	1.4	Dissolved and stable for 21 days

View Article Online
DOI: 10.1039/D6TA01059H

2	0.55 : 1	1.4	Not dissolved
3	0.65 : 1	1.4	Not dissolved
4	0.6 : 1	1	Dissolved and precipitated within 1 day
5	1 : 1	0.1	Not dissolved
6	1 : 1	0.2	Not dissolved
7	1 : 1	0.3	Not dissolved
8	1 : 1	0.4	Dissolved
9	1.82 : 1	0.05	Dissolved and precipitated within 1 day

* The nominal concentration indicates the concentration before accounting for the volume expansion during the dissolution process. Unlike the conventional solution preparation which utilizes volumetric flask, we only used beaker to facilitate the dissolution. On the other hand, volumetric flask requires that the initial solution volume be smaller than the target number when transferring into the flask, and even this small amount of water might result in a discrepancy in the solubility limitation. In that case, we first calculated the required amount of AS and $Ce(SO_4)_2$ for an expected volume (e.g., 1.4 M Ce in 100 mL solution), then added the amount of water which was just enough to dissolve everything, then the final solution volume (114 mL) was measured and recalibrate the actual concentration: 1.4 x 100/114 = 1.23 M.

Physicochemical Characterization. The XANES spectrum of 1.23 M $Ce(SO_4)_2$ in 1.05 M AS (Fig. 1A) displayed whiteline peaks at 5730.0 and 5737.5 eV consistent with Ce(IV). The peak at 5737.5 eV had greater intensity than at 5730 eV, similar to solid $Ce(SO_4)_2$ and distinct from CeO_2. The peak intensity ratio of CeO_2 is similar for crystalline and amorphous forms[30,31], as well as $Ce(OH)_4$[32], consistently distinct from Ce(IV) in the electrolyte solution, which also had a more pronounced pre-edge feature at 5720 eV and lacked the shoulder at 5726.5 eV found in CeO_2 (SI Appendix, Fig. S2A). The intensity minimum at 5732.5 eV was deeper for $Ce(SO_4)_2$ dissolved in AS compared to solid $Ce(SO_4)_2$ (SI Appendix, Fig. S2B), similar to what is reported for dissolved 0.1 M Ce(IV) in 2 M H_2SO_4[33]. The spectrum of $Ce(SO_4)_2$ dissolved in AS is clearly distinct from the trivalent sulfate, $Ce_2(SO_4)_3$ (SI Appendix, Fig. S2C). A linear-combination fit of the XANES spectrum of 1.23 M $Ce(SO_4)_2$ in 1.05 M AS to the spectra of the standards yielded 99.1±0.4% $Ce(SO_4)_2$ and 0.9±0.4% $Ce_2(SO_4)_3$, demonstrating that cerium in solution is predominantly >99%

View Article Online
DOI: 10.1039/D6TA01059H

Ce(IV) (SI Appendix, Fig. S2D). The small Ce(III) component may be a fitting artifact needed to account for the spectral differences between dissolved and solid-phase $Ce(SO_4)_2$, as was previously observed[33]. This demonstrated that Ce(IV) dissolved in AS electrolyte occurs in a similar coordination state as in a H_2SO_4 electrolyte and did not form oxide or hydroxide phases. Raman spectra for different Ce(IV) and blank solutions are shown in Fig. 1B. The original spectra were normalized based on the peak intensity of silicon wafer, which occurred at 520 cm^{-1}. A totally symmetric ν_1-SO_4^{2-} peak located at around 980 cm^{-1} representing unassociated SO_4^{2-} could be observed for blank AS solution, which is consistent with previous literature that AS solution is an ideal model for a "free" sulfate system[34]. After $Ce(SO_4)_2$ was dissolved into AS, the ν_1-SO_4^{2-} peak intensity decreased and completely disappeared at higher $Ce(SO_4)_2$ concentrations, and no HSO_4^--related peak was generated, indicating an interaction between sulfate and Ce^{4+}. Another bending mode, ν_4-SO_4^{2-}, located at 615 cm^{-1} in AS solution, showed a significant blueshift to 665 cm^{-1}, as presented in Fig. 1B. A previous study on supersaturated $MgSO_4$ solution has shown that a similar blueshift is related to the formation of contact ion pairs (CIPs)[35]. This finding implies that instead of the total sulfate species concentration, an efficient binding between sulfate species and Ce(IV) is essential for obtaining a supersaturated Ce(IV) solution. On the other hand, when the concentration of $Ce(SO_4)_2$ was fixed at 0.123 M and supporting electrolyte was varied, the ν_1-SO_4^{2-} peak intensity of $Ce(SO_4)_2$ in AS solution was most prominent, indicating a higher degree of free SO_4^{2-} (SI Appendix, Fig. S3). The spectrum of $Ce(SO_4)_2$ in H_2SO_4 was nearly identical to that of H_2SO_4, which presented no ν_1-SO_4^{2-} peak but a tiny HSO_4^- one at around 1047 cm^{-1}. Neither free SO_4^{2-} nor HSO_4^- was present when $Ce(SO_4)_2$ was dissolved into water, indicating a strong interaction between sulfate and Ce(IV). But the fact that the solubility of $Ce(SO_4)_2$ in water was limited (less than 0.7 M) suggests that the complex stability is highly sensitive to the structure.

View Article Online
DOI: 10.1039/D6TA01059H

The UV-Vis spectra of Ce(IV) in AS and H_2SO_4 are depicted in Fig. 1C, where the Ce(IV) concentration had to be diluted for about 1000 times to obtain clear absorption peaks. With a significant difference in pH value (3.71 in AS vs. -0.02 in H_2SO_4), a clear redshift of absorption peak from 272 to 317 nm was found after AS was substituted by H_2SO_4. A consistent redshift was observed when the supporting electrolyte consisted of different ratios of AS and H_2SO_4 (Fig. 1D). Likewise, Ce(IV) has been found to be complexed more strongly with sulfate species in H_2SO_4 than methanesulfonate in CH_3SO_3H with an absorption peak of 320 vs. 210 nm[33], indicating a stronger complexation with a shift toward longer wavelength. In Fig. 1D, as the ratio between AS and H_2SO_4 was decreased from infinity (only AS) to zero (only H_2SO_4), the pH was lowered while the sulfate species concentration was fixed. The redshift suggests that the binding affinity between Ce(IV) and sulfate species is higher in a low-pH environment.

View Article Online
DOI: 10.1039/D6TA01059H

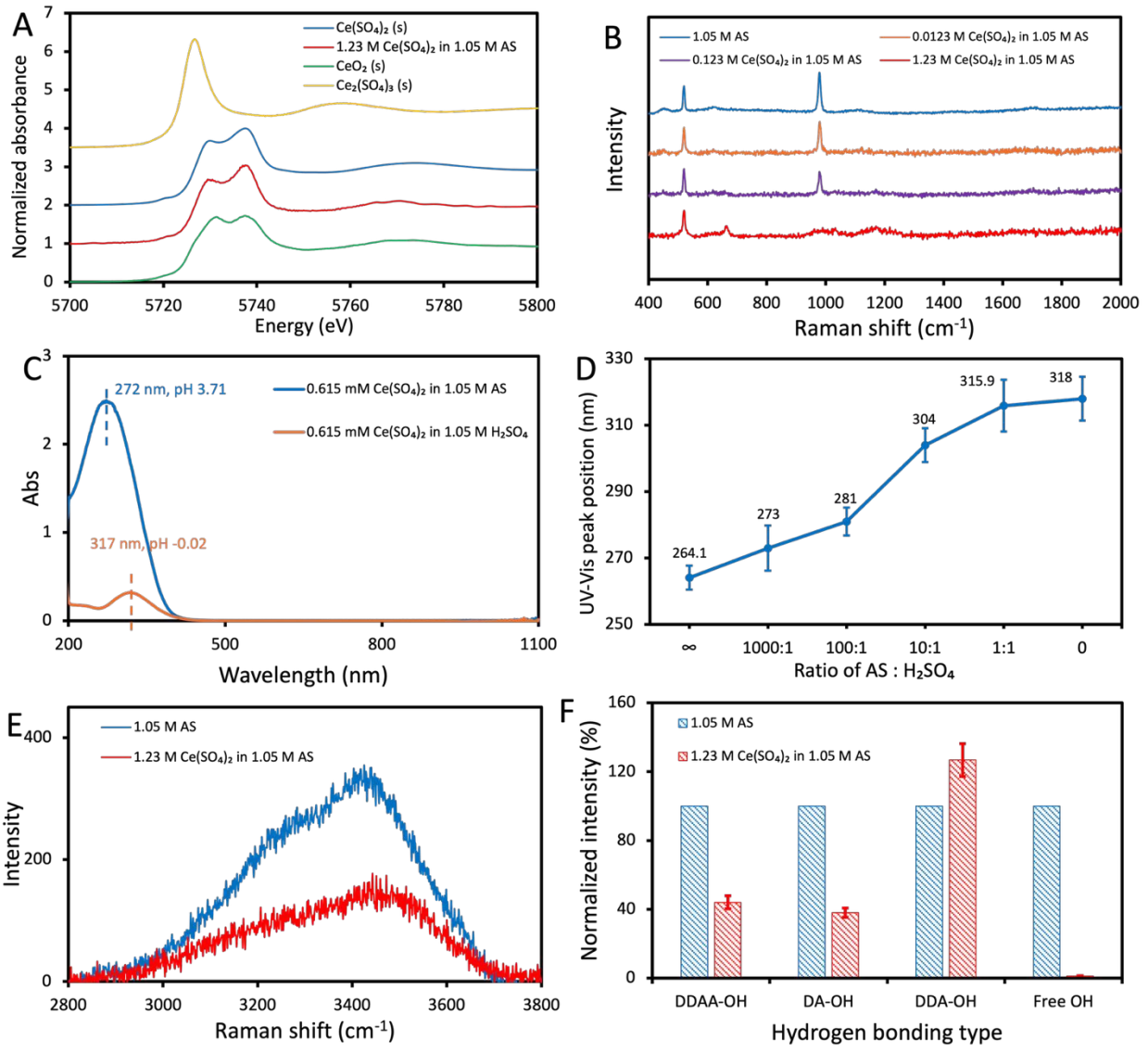

Fig. 1. (A) Ce L_{III}-edge XANES spectra of 1.23 M $Ce(SO_4)_2$ in 1.05 M AS solution compared to $Ce(SO_4)_2$, $Ce_2(SO_4)_3$ and CeO_2 standards; (B) Low-frequency Raman spectra of different concentrations of $Ce(SO_4)_2$ in 1.05 M AS; (C) UV-Vis spectra of 0.615 mM $Ce(SO_4)_2$ in AS and H_2SO_4; (D) UV-Vis absorption peak of 0.3075 mM $Ce(SO_4)_2$ in solutions with different ratios of AS to H_2SO_4 (SA); (E) High-frequency Raman spectra of 1.05 M AS and 1.23 M $Ce(SO_4)_2$ in 1.05 M AS; (*F*) Intensity of hydrogen bonding after 1.23 M $Ce(SO_4)_2$ was dissolved in 1.05 M AS.

Ce(IV) Hydrolysis and Complexation. The complexation between Ce and anions, especially in acidic supporting electrolytes, has been studied extensively [36-38]. In some recent studies, it has been found that in H_2SO_4, Ce(IV) tends to complex with HSO_4^- and the dominant structure is $[Ce(IV)(H_2O)_6(HSO_4)_3]^+$ [22]. In aqueous solutions containing sulfate species, the speciation

View Article Online
DOI: 10.1039/D6TA01059H

relationship between SO_4^{2-} and HSO_4^- is influenced by the dissociation equilibrium constants of H_2SO_4, and HSO_4^- is the dominant species when pH is low, i.e., the dissociation of first proton in H_2SO_4 is normally considered complete, but that of the second one is sluggish (SI Appendix, section S2.1). Thus, a stable structure is obtained by the complexation between Ce(IV) and HSO_4^- instead of SO_4^{2-}, whose quantity is negligible. In AS solutions, however, SO_4^{2-} would be the dominant species rather than HSO_4^- due to the solution's much higher pH (5.4) and the dissociation of proton in NH_4^+ is unfavorable under neutral and acidic environment (SI Appendix, section S2.2). As tabulated in SI Appendix, Table S1, the pH of AS solution decreased significantly after $Ce(SO_4)_2$ was dissolved, ensuring that most of the SO_4^{2-} ions get protonated to form HSO_4^-. The cause of this dramatic pH reduction upon $Ce(SO_4)_2$ dissolution was further examined.

The hydrolysis of Ce(IV) in aqueous solution has been considered very strong[39]. In an ideal solution where the anions do not complex with Ce(IV), the general reaction for Ce(IV) hydrolysis with water is as follows:

$$Ce^{4+} + iH_2O \leftrightarrow Ce(OH)_i^{4-i} + iH^+ \quad [1]$$

where i is the hydration level with values between 0 and 4. The corresponding equilibrium constant, K_i, is defined as follows:

$$K_i = \frac{[Ce(OH)_i^{4-i}][H^+]^i}{[Ce^{4+}]} \quad [2]$$

Using the values from previous literature[40,41], the speciation abundance of different Ce(IV) compounds as a function of pH was generated (SI Appendix, section S2.3 and Fig. S5). At higher pH, the hydrolysis of Ce(IV) is more prominent, indicating that it should be considered when AS is used as the supporting electrolyte. The Ce(IV) structure (e.g., $[Ce(IV)(H_2O)_6(HSO_4)_3]^+$) proposed in previous studies did not consider this hydrolysis reaction, which could be explained by 1) the pH of supporting electrolyte used in those studies being low enough to retard Ce(IV)

View Article Online
DOI: 10.1039/D6TA01059H

hydrolysis; 2) the Ce(IV) concentration used being very low (e.g., 0.25 mM), making it unnecessary to account for the pH change caused by Ce(IV) hydrolysis[22]. In our study, however, the significant Ce(IV) concentration and the corresponding pH change indicated that a significant amount of Ce(IV) hydrolysis was taking place in the solution. When AS was the only supporting electrolyte, all protons were released by Ce(IV), and the number of protons released by each Ce(IV) was calculated from pH, Ce(IV), and sulfate concentration. Taking the electrolyte with highest Ce(IV) concentration, i.e., 1.23 M $Ce(SO_4)_2$ in 1.05 M AS, as an example, the concentration of total protons was calculated as follows:

$$TOT\ H^+ = TOT\ SO_4 + 10^{-pH2} - 10^{-pH1} = 4.955\ M \quad [3]$$

where pH_1 (5.4) and pH_2 (-0.16) represent pH values before and after $Ce(SO_4)_2$ dissolution, and the term TOT SO_4 represents the protons captured by SO_4^{2-} to form HSO_4^- because the latter is the dominant sulfate species at such a low pH. Then two ratios could be easily obtained:

$$\frac{TOT\ H^+}{TOT\ Ce(IV)} = 4.03 \approx 4 \quad [4]$$

$$\frac{TOT\ SO_4}{TOT\ Ce(IV)} = 2.85 \approx 3 \quad [5]$$

The first ratio indicates that for each Ce(IV), four protons were released due to hydrolysis. The second ratio indicates that a complex where the ratio of Ce(IV) to HSO_4^- (following SO_4^{2-} protonation after Ce(IV) hydrolysis) is three could be attained, which coincides with previous investigation[22]. The existence of strong hydrolysis with water is supported by the Raman spectra signals at high Raman shift which represents OH vibrations and hydrogen bonding in water molecules. As shown in Fig. 1E, in a Raman shift range between 2800 to 3800 cm^{-1}, the overall intensity after $Ce(SO_4)_2$ dissolution was significantly lower than that of AS solution. In this range, the Raman spectrum of water can be deconvoluted into five bands centered at 3004, 3227, 3431, 3565, and 3633 cm^{-1}, respectively (details in SI Appendix, section S2.4)[42]. However, it has been

View Article Online
DOI: 10.1039/D6TA01059H

reported that NH_4^+ presents two stretching bands at 3061 and 3131 cm^{-1} [43]. Since the percentage of water hydrogen bonding at 3004 cm^{-1} (single donor-double acceptor, DAA) is very small, the deconvolution was still performed based on all five bands, but the quantitative comparison was made by excluding the one at 3004 cm^{-1}. The deconvoluted results are shown in SI Appendix, Fig. S6 and the intensity of other four types of hydrogen bonding was normalized based on the peak area of AS solution, as illustrated in Fig. 1F. The intensity of double donor-double acceptor (DDAA, 3227 cm^{-1}) and single donor-single acceptor (DA, 3431 cm^{-1}) was reduced to less than 50 %, and that of free OH vibrations (3633 cm^{-1}) was nearly eliminated. The notable decrease of hydrogen bonding intensity indicates that water molecules are more structured by hydrolysis and complexation. Hence, we propose a new pathway for Ce(IV) dissolution and complexation in AS solutions that combines both hydrolysis with water and complexation with HSO_4^-, to form the possible complex $[Ce(OH)_4(HSO_4^-)_3]^{3-}$, as depicted in Fig. 2. The bonding strength between Ce(IV) and HSO_4^- becomes weaker due to the negative charge carried by hydroxide (OH^-), reducing the likelihood of Ce(IV)-sulfate precipitation and thus increasing Ce(IV) solubility. Similar calculations and analysis were performed on all three supporting electrolytes (water, H_2SO_4, and AS) with a lower Ce(IV) concentration (0.123 M) (SI Appendix, section S2.5). In water, the ratio of Ce to sulfate was fixed at 1:2, suggesting that the stable structure which requires a ratio of 1:3 was never achieved. As a result of that, the solution would tend to precipitate relatively quickly, as shown in SI Appendix, Fig. S7. In H_2SO_4, the majority of total protons came from the acid itself instead of Ce(IV) hydrolysis, revealing that hydrolysis was thermodynamically unfavorable. At a relatively low concentration (e.g., 0.123 M Ce), the sulfate from $Ce(SO_4)_2$ could be fully protonated by H_2SO_4 and Ce(IV) hydrolysis leading to the formation of stable Ce(IV) complex structures (the ratio of sulfate to Ce is much higher than 3). As the concentration of $Ce(SO_4)_2$ or

View Article Online
DOI: 10.1039/D6TA01059H

294 H_2SO_4 is increased, however, free SO_4^{2-} starts to be nonnegligible in the system, which competes
295 with HSO_4^- to bind with Ce(IV) and precipitate as $Ce(SO_4)_2$ solid. This is a manifestation of the
296 common ion effect wherein the $Ce(SO_4)_2$ solubility decreases as H_2SO_4 concentration increases[14].
297 Notably, the calculation results for 0.123 M $Ce(SO_4)_2$ in 1.05 M AS suggest that eight protons
298 were released, much higher than the highest number from hydrolysis with water (four). Thus, at
299 this intermediate Ce(IV) concentration, NH_4^+ can be hydrolyzed by Ce(IV) to release protons and
300 a complex with $-NH_3$ can be formed. The participation of NH_4^+ supports the earlier observation
301 that a same concentration of $Ce(SO_4)_2$ was not able to dissolve in Na_2SO_4. The presence of free
302 SO_4^{2-} in this solution (pH = 1.63) implies that the solution was not stable and would precipitate,
303 and this was indeed observed experimentally as shown in SI Appendix, Fig. S8. At even higher
304 Ce(IV) concentrations (1.23 M), the protons from water hydrolysis were abundant and ammonium
305 was re-protonated and detached. Based on the analysis above, a low pH environment which results
306 in HSO_4^- being the dominant species of sulfate is the key for a stable $Ce(SO_4)_2$ solution. Ce(IV)
307 concentration and stability was found to be a function of the pH and increases at low pH but only
308 if the acidity is generated by Ce(IV) hydrolysis instead of the addition of any acidic supporting
309 electrolyte. Thus, the improved solubility is a result of the complementary and synergistic effects
310 of Ce(IV) hydrolysis and complexation. We herein propose a new criterion for $Ce(SO_4)_2$ solubility
311 in aqueous solution: the content of sulfate does not decide the solubility, but a favorable complex
312 between Ce(IV) and other species (i.e., water and HSO_4^-) plays the key role. The low pH of the
313 final solution is a prerequisite since it makes sure that HSO_4^- is the dominant sulfate species, but
314 the low pH should come from Ce(IV) hydrolysis (e.g., in AS) to form $Ce(OH)_i^{4-i}$ intermediates and
315 not the solvent itself (e.g., H_2SO_4). More quantitative study (e.g., density function theory

View Article Online
DOI: 10.1039/D6TA01059H

calculation and extended X-ray absorption fine structure) will be conducted in our future work to prove the Ce(IV) complex coordination.

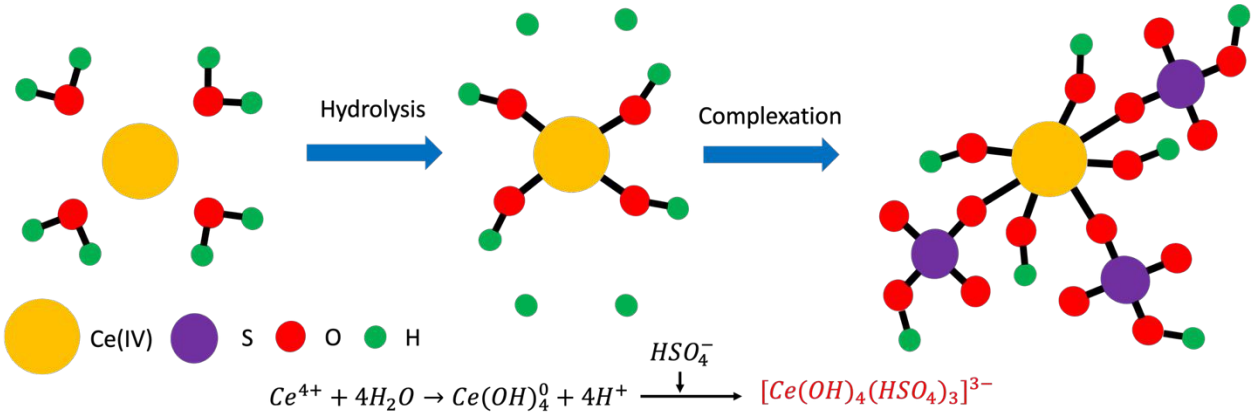

Fig. 2. Schematic of Ce(IV) hydrolysis and possible complexation coordination in AS solution.

Electrochemical Characterization. In this study, CP and CF were selected as candidates for electrodes on Ce side. In our previous study[51], CF was proved to get degraded by methanesulfonic acid-based Ce(IV) electrolyte, shown by the vanishment of anodic peak and shift of cathodic peak towards the negative direction after CF was immersed into Ce electrolyte for 24 h. Similar stability test was conducted in this study. The CVs revealed that with the AS supporting electrolyte, both peak positions and redox currents on CF electrodes remained stable after immersion into Ce(IV) for 24 h, as shown in Fig. 3B. The decrease of the oxidizing nature of Ce(IV) in AS (compared to CH_3SO_3H supported electrolytes) was attributed to the stronger complexation with sulfate species and hydrolysis with water, which made Ce(IV) more stable and harder to get reduced chemically. The comparison between CVs of CP and CF in Figs. 3A and 3B and SI Appendix, Table S2 demonstrates significantly performance differences: better reversibility on CP (smaller peak separation) and enhanced reactivity on CF (higher peak currents)[44]. The improved apparent kinetics on CF is attributed to its higher surface area, while the increased reversibility on CP is attributed to differences in surface functionalization (additional fundamental studies are needed

View Article Online
DOI: 10.1039/D6TA01059H

but outside the scope of this study). Similarly raw CP and HT CP, raw CF and HT CF were immersed in Ce(IV)-AS electrolyte, and both anodic and cathodic peak currents dropped significantly for HT CF, indicating poor oxidative stability, as depicted in Figs. 3D and 3F. We hypothesize that the deterioration of HT CF in Ce(IV) electrolyte was facilitated by the oxygen functional groups produced on the surface during thermal pretreatment. Based on these results, CF was selected as the electrode for Ce side.

The CVs of CF at different scan rates were analyzed to obtain the diffusion coefficient of the Ce complexes and the reaction rate constants. As shown in Fig. 3C, the peak potential separations at all scan rates were higher than 59 mV and increased with scan rate, suggesting that the Ce redox reaction was not readily reversible[45]. The N-S equation was used to calculate D_0 as follows:

$$i_p = 2.99 \times 10^5 n^{3/2} \alpha^{1/2} A C_0 D_0^{1/2} \nu^{1/2} \quad [6]$$

where i_p is the peak current, n is the number of electrons transferred during the reaction, α is the electron transfer coefficient, A is the electrode surface area, C_0 is the Ce concentration in bulk electrolyte, D_0 is the diffusion coefficient, and ν is the scan rate[26,27]. The transfer coefficient, α, was calculated using the following equation:

$$\alpha = \frac{1.86RT}{F(E_p - E_{\frac{p}{2}})} \quad [7]$$

where R is the universal gas constant (8.314 J·mol^{-1}·K^{-1}), T is the temperature, F is the Faraday's constant (96485 C·mol^{-1}), E_p is the peak potential, and $E_{p/2}$ is the half-peak potential[46]. The α values are tabulated in SI Appendix, Table S3, and a clear deviation from 0.5 indicates that the reaction is irreversible. Similarly, the K-K equation was used for obtaining k_0 as follows:

$$k_0 \exp\left[\frac{\alpha n F}{RT}\left(E_p - E_0\right)\right] = 2.18\left[\frac{D_0 \alpha n F \nu}{RT}\right]^{\left(\frac{1}{2}\right)} \quad [8]$$

View Article Online
DOI: 10.1039/D6TA01059H

where k_0 is the standard rate constant, E_0 is the standard electrode potential, which was calculated from the average of cathodic and anodic peak potentials. The corresponding N-S and K-K plots are depicted in SI Appendix, Fig. S9, from which the slope was used to calculate the value of D_0 and k_0, as tabulated in SI Appendix, Table S4.

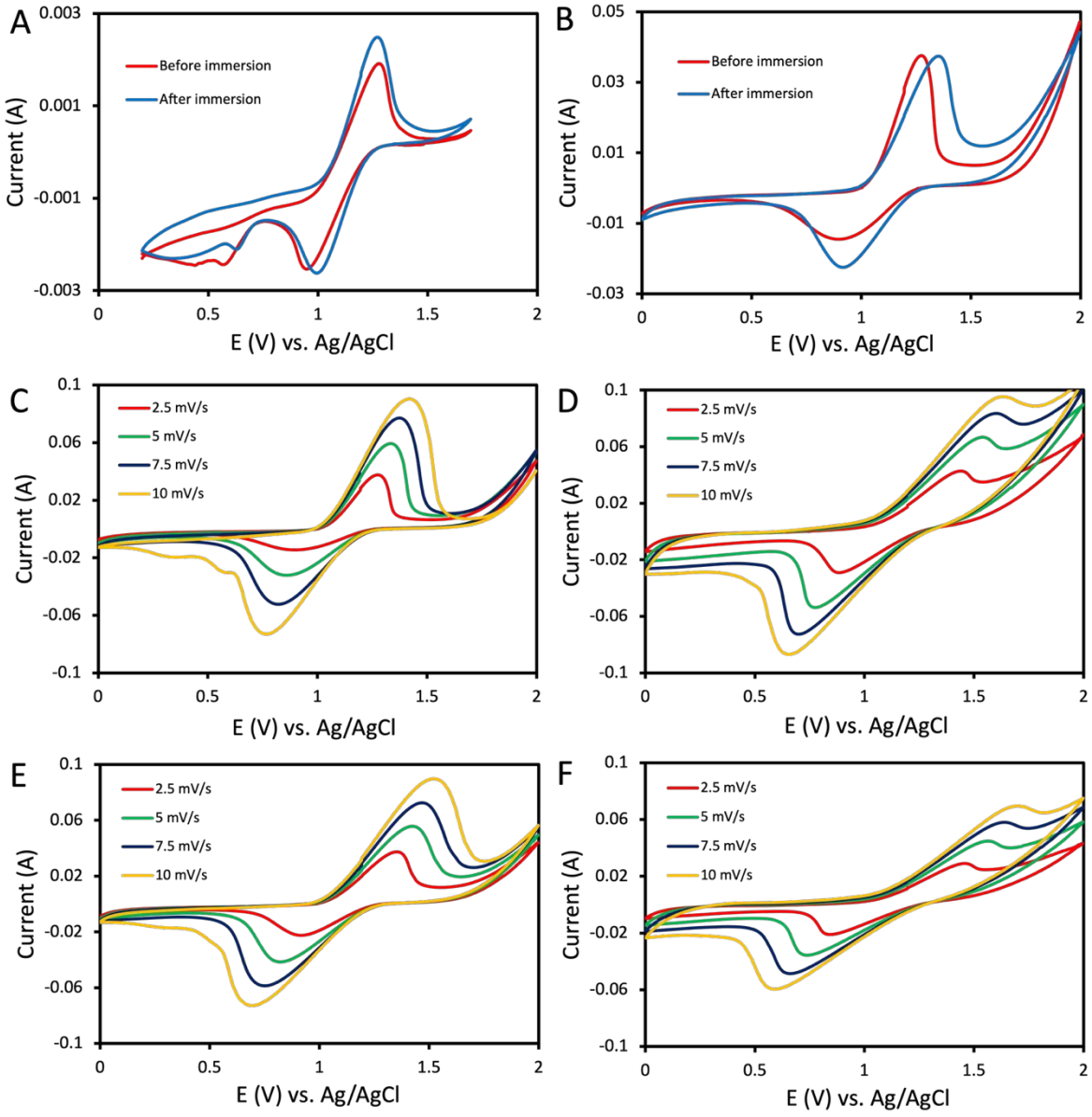

Fig. 3. CVs of different carbon electrodes with 0.123 M $Ce(SO_4)_2$ in 1.05 M AS: (A) CP, before & after immersion, 2.5 mV/s; (B) CF, before & after immersion, 2.5 mV/s; (C) CF, before immersion; (D) HT CF, before immersion; (E) CF, after immersion; (F) HT CF, after immersion.

View Article Online
DOI: 10.1039/D6TA01059H

Ti-Ce RFBs Test. The optimized Ce electrolyte was tested on CF electrodes in a Ti-Ce RFB. First the Ti electrolyte was reduced to Ti(III) in a V-Ti cell configuration to enable us to cycle it with Ce(IV). The theoretical time for a single full charge of the V-Ti RFB was calculated to be 1.32 h, which was close to the actual duration (1.2 h), suggesting that all Ti(IV) was reduced to Ti(III) (SI Appendix, section S2.6). The QPEK-C-TMA AEM utilized in this study has been applied to several RFB systems with Ce, Ti, and V [12,51-53], and the permselectivity was proved excellent without unwanted crossover. The high frequency resistance (HFR), which includes ionic or contact resistance of different components in RFB[47], is shown in Fig. 4A for the initial stage of Ti-Ce RFBs cycling. A significant fluctuation of HFR during discharge was observed with a peak value higher than 500 mOhm at the beginning of discharge process. To put this in perspective, the HFR in all-V RFB cells is typically around 50 mOhm and thus is not a major performance limiter[48,49]. When a constant-current plus constant-voltage protocol was used, the large ohmic polarization at the early phase of discharge would bring the cell potential to the cut-off condition immediately, forcing the system into the next constant-voltage stage and lowering the energy efficiency (EE) (Fig. 4B). As the discharge proceeded, however, the HFR decreased to a more reasonable lever (100 mOhm), which led to a remarkable phenomenon: the discharge current density in constant-voltage phase was promoted to be more than two times that of constant-current stage (50 mA cm^{-2}), indicating that significant discharge capacity was not utilized in the constant current (CC) stage (Fig. 4C). The hypothesis that this pronounced HFR was due to the precipitation of nanoparticles of Ce(III) stemmed from low solubility of Ce(III) in sulfate environment was found to be incorrect as the HFR was not affected by increases in flowrate that would be expected to sweep away particulate precipitates inside the cell (see HFR as a function of electrolyte flowrate in SI Appendix Fig. S11). The conductivity of both Ce and Ti electrolytes is tabulated in SI Appendix, Table S5,

View Article Online
DOI: 10.1039/D6TA01059H

and the values were comparable with electrolytes of other RFBs[50]. Thus, the HFR increase was traced back to the Ce(IV) complex's structure in solution. As discussed earlier, Ce(IV) was bound with HSO_4^- to form a complex that is much larger than HSO_4^-. Since an AEM was used in RFB tests, the transport of negative charge through the separator was required to maintain the electroneutrality. Nonetheless, the substantial steric bulk and local positive charge of Ce(IV) would hamper this process, resulting in a high HFR. To discuss the effects of this complex on electrochemical reaction kinetics, the solvent reorganization energy, λ, which is the amount of energy required to re-organize the solvent configuration of the reactant to the state of product, using Equation 9[55]. In this equation, α is electron transfer coefficient, F is the Faraday's constant (96485 C mol^{-1}), E_0 is the standard potential of the considered reaction, which is the average of anodic and cathodic peak potential in CV, and ϕ_r is the potential at the plane of the reaction site versus bulk solution. Since the reaction was assumed to occur at the surface of electrode, $E \approx \phi_r$. Take the CV of 10 mV s^{-1} in Figure 3C as an example, where α_c was 0.209, E_0 was 1.1 V. The corresponding solvation overpotential, λ/F, was calculated to be 0.945 V. Given that the difference between the maximum applied potential (2 V) and E_0 was less than the solvation overpotential, the Ce complex is unlikely to be desolvated, indicating that Ce(IV) complex was undergoing an outer-sphere electron transfer. In other words, the active redox couple at the positive electrode consisted of Ce complexes at different oxidation states rather than desolvated Ce^{4+} and Ce^{3+}. The fact that the active species was in a bulky complex form also explains the steric bulk inducing high HFR. As the discharge advanced, more Ce(IV) was reduced to Ce(III) and free HSO_4^- was gradually released owing to the deficiency of Ce(III) in complexing with sulfate. Consequently, the HFR fell as the ionic charge carrier changed from the Ce(IV) complex to the far less bulky HSO_4^- ion. This

View Article Online
DOI: 10.1039/D6TA01059H

postulation successfully correlates the HFR behavior with the proposed Ce(IV) structure in AS solution.

$$\alpha = 0.5 + \frac{F}{4\lambda}(E - E_0 - \phi_r)$$

In order to make sure that the majority of discharge is concentrated in constant-current phase, a short (2 mins) constant-voltage (CV) of 2 V segment was added before the constant-current segment with the intention of attenuating the HFR so that the following constant-current stage was terminated by mass transport polarization instead of ohmic polarization. As depicted in Figs. 4E and 4F, a discharge curve dominated by constant-current phase was achieved with this new protocol, and the test showed an average EE of 70.2% and was operated consistently for more than 12 h. No second plateau was observed in Fig. 4E, further supporting that V was not crossing into Ti side during the pre-charge of V-Ti cell. The move from a typical CC-CV to a CV-CC-CV discharge profile is expected to have minimal impact on eventual grid integration. Grid applications require constant AC power output with frequency matching[56-59]. The battery management system (BMS) and the power conditioning system (PCS) are designed to ensure this and account for the typical constant DC current – constant DC voltage discharge profiles of batteries. The power conditioning systems coupled to a battery typically incorporate a DC-DC converter to ensure that the DC voltage output from the battery is within the optimal input range for the DC-to-AC converter. The AC output in-turn is subject to a grid following (GFL) or grid forming (GFM) control scheme[60]. Thus, these systems will ensure that the AC output to grid will be within acceptable parameters even when a portion of the discharge happens at constant DC voltage. After that, both EE and discharge capacity degraded due to the clogging of tube and flow field channel induced by Ce precipitation (SI Appendix, Fig. S12). The Ce precipitation was detected in CF electrode, too: the weight of CF after cycling test was nearly doubled (SI Appendix,

View Article Online
DOI: 10.1039/D6TA01059H

Table S6), and clear Ce deposition on graphite fiber was observed by scanning electron microscope (SEM) and energy dispersive X-ray (EDX) (SI Appendix, Figs. S13 and S14). However, if the precipitate and clogging inside the cell and tube was removed, the performance degradation was entirely reversed as shown in Fig. 5, proving that the performance degradation was mainly caused by clogging and not by other modes of irreversible capacity fade. The entrance and exit of flow field in this study was already enlarged compared with the conventional design (Fig. S1A), and the RFB test with the conventional flow field was not even able to finish a typical cycle, as shown in Fig. S15. Future work will focus on other strategies to prevent battery failure from clogging (e.g., by increasing channel widths of flow field and porosity of electrodes). Despite that the cycling performance shown here was worse than our previous study using non-AS supporting electrolytes[51,54], the high theoretic energy density (33.0 Ah L^{-1}) still indicates a great potential for further development and application. Some alternative positive electrodes, e.g., Pt-Ti, will also be tested in the future work to examine the role of the oxidative nature of Ce(IV) on the performance of the system. Notably, we have demonstrated diurnal cycling and cycling over several months using carbon felt based positive electrodes with no deleterious effects[12,51,54]. The oxidative nature of Ce(IV) may even serve to sustain catalytic oxygen functional groups on the positive electrode surface (originally generated by thermal treatment).

View Article Online
DOI: 10.1039/D6TA01059H

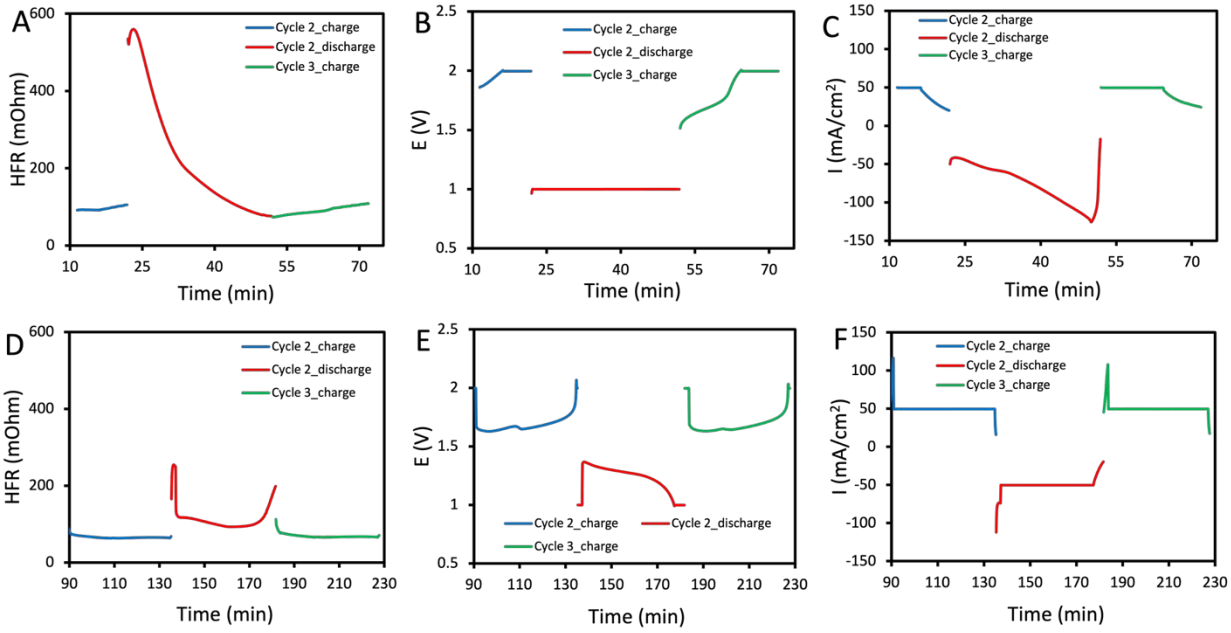

Fig. 4. Ti-Ce RFBs tests: (A) HFR, (B) cell voltage, and (C) current density with constant-current + constant-voltage protocol; (D) HFR, (E) cell voltage, and (F) current density with constant-voltage + constant-current + constant-voltage protocol. Catholyte: 1.23 M $Ce(SO_4)_2$ in 1.05 M AS; anolyte: 1.23 M $TiOSO_4$ in 1.9 M AS after a full reduction to Ti(III).

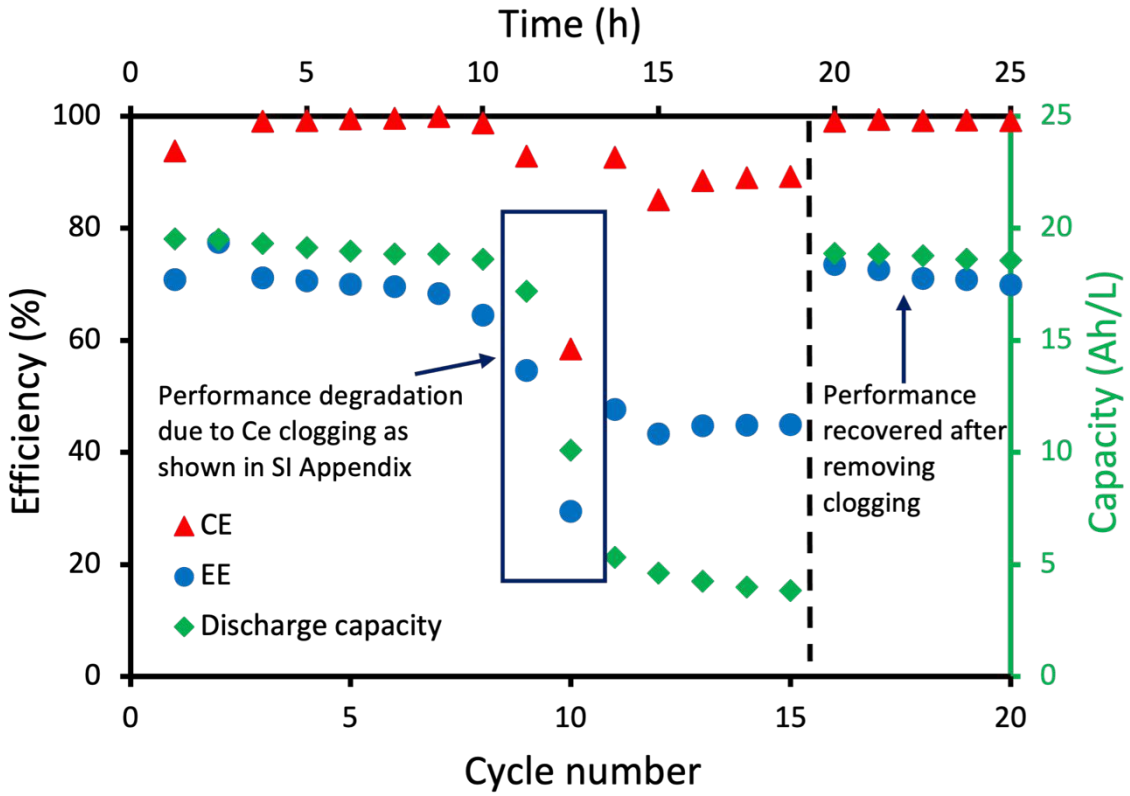

View Article Online
DOI: 10.1039/D6TA01059H

Fig. 5. Ti-Ce RFBs performance with constant-voltage + constant-current + constant-voltage protocol. Clogging removed after 15th cycle. The capacity fade between cycles 8 and 16 was reversible and due to the clogging of the cell tubing and electrode pores by the Ce precipitate as seen in ESI Fig. S12. Original capacity was recovered once the precipitates were washed off into the electrolyte tanks. Catholyte: 1.23 M $Ce(SO_4)_2$ in 1.05 M AS; anolyte: 1.23 M $TiOSO_4$ in 1.9 M AS after a full reduction to Ti(III).

Conclusions

The application of Ce redox couple in RFBs is restricted by the low solubility of Ce. In this work, we develop a supersaturated Ce(IV) electrolyte with 1.23 M of active species enabled by an ammonium sulfate supported electrolyte. Complementary Ce(IV) hydrolysis and complexation was determined to be the primary factor contributing to this high solubility. In the AS solution, Ce(IV) was highly hydrolyzed with water to release protons, which reduce pH and assist in the formation of HSO_4^-, and the strong complexation between Ce(IV) and HSO_4^- results in a stable structure proposed as $[Ce(OH)_4(HSO_4^-)_3]^{3-}$. Notably, the operating current density and associated energy efficiency are higher than comparable cerium-based flow batteries as seen in previous studies[11] while simultaneously operating with a 40% higher Ce specific energy. Ti-Ce RFBs based on this electrolyte exhibited very high specific capacity (practically achieved 19 Ah L^{-1} out of a nominal capacity of 33.0 Ah L^{-1}), energy efficiency over 70% and no irreversible capacity fade, thus making the case for its use in grid scale energy storage.

Author Contributions

J.X.: Conceptualization, data curation, formal analysis, investigation, methodology, validation, visualization, writing-original draft, writing-review & editing; S.S: Conceptualization, formal analysis, methodology, writing-original draft, writing-review & editing; J.G.C.: Data curation, writing-original draft, writing-review & editing; V.R.: Conceptualization, formal analysis, funding

View Article Online
DOI: 10.1039/D6TA01059H

acquisition, methodology, project administration, resources, supervision, validation, visualization, writing-original draft, writing-review & editing.

Conflicts of Interest

The authors currently have no financial interests that may be perceived to influence the conclusions presented in this work. Some of the authors are seeking intellectual property protections on aspects of one or more technologies described in this report through the Office of Technology and Management (OTM) at Washington University in St. Louis (WUSTL).

Data Availability Statement

All of the data associated with these studies are represented in the manuscript and supplemental information. The raw data are available from the corresponding author upon reasonable request. The references cited in the Supplementary Information (SI) have been listed at the bottom of the reference section.

Acknowledgements

J.X., S.S., and V.R. would like to acknowledge the support of the Advanced Research Projects Agency-Energy (ARPA-E), the US Department of Energy under award no. DE-AR0000768 as part of the Integration and Optimization of Novel Ion Conducting Solids (IONICS) program and the McKelvey School of Engineering, Washington University in St. Louis and the Roma B. & Raymond H. Wittcoff Distinguished University Professorship. Yin-Yuan Huang is thanked for assistance with Raman spectroscopy measurement. The work of J.G.C. was supported by the U.S.

View Article Online
DOI: 10.1039/D6TA01059H

Department of Energy, Office of Science, Office of Basic Energy Sciences, Critical Minerals and Materials program under Award Number DE-SC0022213. Elaine Flynn is thanked for assistance with sample preparation for XANES analysis.

View Article Online
DOI: 10.1039/D6TA01059H

Reference

1. M. Shoaib, P. Vallayil, N. Jaiswal, P. I. V. Suba, S. Sankararaman, K. Ramanujam and V. Thangadurai, Advances in redox flow batteries - A comprehensive review on inorganic and organic electrolytes and engineering perspective. *Adv. Energy Mater.*, 2024, **14**, 2400721.
2. Z. Hou, X. Chen, J. Liu, Z. Huang, Y. Chen, M. Zhou, W. Liu and H. Zhou, Towards a high efficiency and low-cost aqueous redox flow battery: A short review. *J. Power Sources*, 2024, **601**, 234242.
3. R. Huang, S. Liu, Z. He, W. Zhu, G. Ye, Y. Su, W. Deng and J. Wang, Electron-deficient sites for improving V^{2+}/V^{3+} redox kinetics in vanadium redox flow batteries. *Adv. Funct. Mater.*, 2022, **32**, 2111661.
4. V. Fernandez, Rare-earth elements market: A historical and financial perspective. *Resour. Policy*, 2017, **53**, 26-45.
5. S. Fahed, R. Pointecouteau, M. Aouine, A. Boréave, S. Gil, V. Meille, P. Bazin, O. Toulemonde, A. Demourgues, M. Daturi and P. Vernoux, Pr-rich cerium-zirconium-praseodymium mixed oxides for automotive exhaust emission control. *Appl. Catal. A Gen*., 2022, **644**, 118800.
6. T. S. Lima, M. C. Santos, A. J. Motheo, Electrochemical generation of hydrogen peroxide using cerium oxide nanostructures supported on graphene: Synthesis, characterization, and application in wastewater treatment. *Electrochim. Acta*, 2025, **521**, 145931.
7. L. C. Chen, T. Luo, Z. Y. Cao, P. Dalladay-Simpson, G. Huang, D. Peng, L. L. Zhang, F. A. Gorelli, G. H. Zhou, H. Q. Lin and X. J. Chen, Synthesis and superconductivity in yttrium-cerium hydrides at high pressures. *Nat. Commun*., 2024, **15**, 1809.
8. P. Wei, Y. Wang, H. Feng, F. Zhang, Z. Ji, K. Zhang, Q. Zhang, L. Jiang, Y. Qian and Y. Fu, Gene-engineered cerium-exosomes mediate atherosclerosis therapy through remodeling of the inflammatory microenvironment and DNA damage repair. *Small*, 2024, **20**, 2404463.
9. M. Shahbaz, S. Sharif, A. Shahzad, Z. S. Şahin, B. Riaz and S. Shahzad, Enhanced electrochemical performance of cerium-based metal organic frameworks derived from pyridine-2,4,6-tricarboxylic acid for energy storage devices. *J. Energy Storage*, 2024, **88**, 111463.
10. Z. Xie, Q. liu, Z. Chang and X. Zhang, The developments and challenges of cerium half-cell in zinc–cerium redox flow battery for energy storage. *Electrochim. Acta*, 2013, **90**, 695-704.
11. L. F. Arenas, F. C. Walsh and C. P. De León, Wiley, 2003, "Zinc–cerium and related cerium-based flow batteries: Progress and challenges" In *Flow Batteries*, 1st ed., edited by Christina Roth, Jens Noack, and Maria Skyllas-Kazacos.
12. S. Sankarasubramanian, Y. Zhang and V. Ramani, Methanesulfonic acid-based electrode-decoupled vanadium–cerium redox flow battery exhibits significantly improved capacity and cycle life. *Sustain. Energy* Fuels, 2019, **3**, 2417-2425.
13. F. C. Walsh, C. P. de Léon, L. Berlouis, G. Nikiforidis, L. F. Arenas-Martínez, D. Hodgson and D. Hall, The development of Zn–Ce hybrid redox flow batteries for energy storage and their continuing challenges. *ChemPlusChem*, 2015, **80**, 288-311.
14. A. Paulenova, S. E. Creager, J. D. Navratil and Y. Wei, Redox potentials and kinetics of the Ce^{3+}/Ce^{4+} redox reaction and solubility of cerium sulfates in sulfuric acid solutions. *J. Power Sources*, 2002, **109**, 431-438.
15. R. M. Spontnitz, R. P. Kreh, J. T. Lundquist and P. J. Press, Mediated electrosynthesis with cerium (IV) in methanesulphonic acid. *J. Appl. Electrochem*., 1990, **20**, 209-215.
16. Y. Li, P. Geysens, X. Zhang, J. Sniekers, J. Fransaer, K. Binnemans and I. F. J. Vankelecom, Cerium-containing complexes for low-cost, non-aqueous redox flow batteries (RFBs). *J. of Power Sources*, 2020, **450**, 227634.

View Article Online
DOI: 10.1039/D6TA01059H

17. E. S. Beh, D. D. Porcellinis, R. L. Gracia, K. T. Xia, R. G. Gordon and M. J. Aziz, A neutral pH aqueous organic–organometallic redox flow battery with extremely high capacity retention. *ACS Energy Lett.*, 2017, **2**, 639-644.
18. L. Y. Cao, M. Skyllas-Kazacos, C. Menictas and J. Noack, A review of electrolyte additives and impurities in vanadium redox flow batteries. *J. Energy Chem*., 2018, **27**, 1269-1291.
19. M. Skyllas-Kazacos, C. Peng and M. Cheng, Evaluation of precipitation inhibitors for supersaturated vanadyl electrolytes for the vanadium redox battery. *Electrochem. Solid State Lett*., 1999, **2**, 121-122.
20. N. Kausar, A. Mousa and M. Skyllas-Kazacos, The effect of additives on the high-temperature stability of the vanadium redox flow battery positive electrolytes. *ChemElectroChem*, 2016, **3**, 276-282.
21. N. W. Pettinger, R. E. A. Williams, J. Q. Chen and B. Kohler, Crystallization kinetics of cerium oxide nanoparticles formed by spontaneous, room-temperature hydrolysis of cerium(IV) ammonium nitrate in light and heavy water. *Phys. Chem. Chem. Phys*., 2017, **19**, 3523-3531.
22. C. A. Buchanan, D. Herrera, M. Balasubramanian, B. R. Goldsmith and N. Singh, Unveiling the cerium(III)/(IV) structures and charge-transfer mechanism in sulfuric acid. *JACS Au*, 2022, **2**, 2742-2757.
23. E. P. Jahrman, W. M. Holden, A. S. Ditter, D. R. Mortensen, G. T. Seidler, T. T. Fister, S. A. Kozimor, L. F. J. Piper, J. Rana, N. C. Hyatt and M. C. Stennett, An improved laboratory-based x-ray absorption fine structure and x-ray emission spectrometer for analytical applications in materials chemistry research. *Rev. Sci. Instrum*., 2019, **90**, 024106.
24. B. Ravel, M. Newville, ATHENA, ARTEMIS, HEPHAESTUS: data analysis for X-ray absorption spectroscopy using IFEFFIT. *J. Synchrotron Radiat*., 2005, **12**, 537-541.
25. M. Newville, IFEFFIT : interactive XAFS analysis and FEFF fitting. *J. Synchrotron Radiat.*, 2001, **8**, 322-324.
26. R. S. Nicholson and I. Shain, Theory of stationary electrode polarography: Single scan and cyclic methods applied to reversible, irreversible, and kinetic systems. *Anal. Chem*., 1964, **36**, 706–723.
27. R. S. Nicholson, Theory and application of cyclic voltammetry for measurement of electrode reaction kinetics. *Anal. Chem*., 1965, **37**, 1351–1355.
28. R. J. Klingler and J. K. Kochi, Electron-transfer kinetics from cyclic voltammetry. Quantitative description of electrochemical reversibility. *J. Phys. Chem*., 1981, **85**, 1731-1741.
29. S. Yun, J. Parrondo, and V. Ramani, Derivatized cardo-polyetherketone anion exchange membranes for all-vanadium redox flow batteries. *J. Mater. Chem. A*, 2014, **2**, 6605-6615.
30. A. M. Shahin, F. Grandjean, G. J. Long and T. P. Schuman, Cerium L_{III}-Edge XAS investigation of the structure of crystalline and amorphous cerium oxides. *Chem. Mat*., 2005, **17**, 315-321.
31. P. Nachimuthu, W.-C. Shih, R.-S. Liu, L.-Y. Jang and J.-M. Chen, The study of nanocrystalline cerium oxide by X-Ray absorption spectroscopy. *J. Solid State Chem*., 2000, **149**, 408-413.
32. H. Yoshida, L. Yuliati, T. Hamajima, and T. Hattori, Valence of highly dispersed cerium oxide species on silica quantitatively estimated by Ce L_{III}-edge XANES. *Mater. Trans*., 2004, **45**, 202-2067.
33. C. A. Buchanan, E. Ko, S. Cira, M. Balasubramanian, B. R. Goldsmith and N. Singh, Structures and free energies of cerium ions in acidic electrolytes. *Inorg. Chem*., 2020, **59**, 12552-12563.

View Article Online
DOI: 10.1039/D6TA01059H

598 34. Y. H. Zhang and C. K. Chan, Understanding the hygroscopic properties of supersaturated
599 droplets of metal and ammonium sulfate solutions using Raman spectroscopy. *J. Phys. Chem. A*,
600 2002, **106**, 285-292.
601 35. Y. H. Zhang and C. K. Chan, Study of contact ion pairs of supersaturated magnesium sulfate
602 solutions using Raman scattering of levitated single droplets. *J. Phys. Chem. A*. 2000, **104**, 9191-
603 9196.
604 36. L. F. Arenas, C. Ponce de León and F. C. Walsh, Electrochemical redox processes involving
605 soluble cerium species. *Electrochim. Acta*, 2016, **205**, 226-247.
606 37. W. Schmickler, R. R. Nazmutdinov, Q. Wang and W. A. Daoud, Electrochemistry of
607 Ce(IV)/Ce(III) redox couples in mixed solutions for aqueous flow battery: Experimental and
608 molecular modelling study. *Electrochim. Acta*, 2021, **368**, 137601.
609 38. M. A. Brown, A. Paulenova and A. V. Gelis, Aqueous complexation of thorium(IV),
610 uranium(IV), neptunium(IV), plutonium(III/IV), and cerium(III/IV) with DTPA. *Inorg. Chem*.,
611 2012, **51**, 7741-7748.
612 39. R. Marsac, F. Réal, N. L. Banik, M. Pédrot, O. Pourret and V. Vallet, Aqueous chemistry of
613 Ce(IV): estimations using actinide analogues. *Dalton Trans*., 2017, **16**, 13553-13561.
614 40. S. A. Hayes, P. Yu, T. J. O'Keefe, M. J. O'Keefe and J. O. Stoffer, The phase stability of
615 cerium species in aqueous systems: I. E-pH diagram for the system. *J. Electrochem. Soc*., 2002,
616 **149**, C623-C630.
617 41. B. Bouchaud, J. Balmain, G. Bonnet and F. Pedraza, pH-distribution of cerium species in
618 aqueous systems. *J. Rare Earths*, 2012, **30**, 559-562.
619 42. Q. Sun, The Raman OH stretching bands of liquid water. *Vib. Spectrosc*., 2009, **51**, 213-217.
620 43. M. Jordanov and R. Zellner, Investigations of the hygroscopic properties of ammonium sulfate
621 and mixed ammonium sulfate and glutaric acid micro droplets by means of optical levitation and
622 Raman spectroscopy. *Phys. Chem. Chem. Phys*., 2006, **8**, 2759-2764.
623 44. M. Park, E. S. Beh, E. M. Fell, Y. Jing, E. F. Kerr, D. D. Porcellinis, M. A. Goulet, J. Ryu, A.
624 A. Wong, R. G. Gordon, J. Cho and M. J. Aziz, A high voltage aqueous zinc–organic hybrid flow
625 battery. *Adv. Energy Mater.*, 2019, **9**, 1900694.
626 45. A. J. Bard and L. R. Faulkner, Wiley, ed.2, 2000, Electrochemical Methods: Fundamentals and
627 Applications.
628 46. C. O. Laoire, S. Mukerjee, K. M. Abraham, E. J. Plichta and M. A. Hendrickson, Influence of
629 nonaqueous solvents on the electrochemistry of oxygen in the rechargeable lithium-air battery. *J.*
630 *Phys. Chem. C*, 2010, **114**, 9178–9186.
631 47. Y. A. Gandomi, D. S. Aaron, J. R. Houser, M. C. Daugherty, J. T. Clement, A. M. Pezeshki,
632 T. Y. Ertugrul, D. P. Moseley and M. M. Mench, Critical review—Experimental diagnostics and
633 material characterization techniques used on redox flow batteries. *J. Electrochem. Soc*., 2018, **165**,
634 A910-A1010.
635 48. Y. Li, J. Bao, M. Skyllas-Kazacos, M. P. Akter, X. Zhang and J. Fletcher, Studies on dynamic
636 responses and impedance of the vanadium redox flow battery. *Appl. Energy*, 2019, **237**, 91-102.
637 49. K. Amini, A. N. Shocron, M. E. Suss and M. J. Aziz, Pathways to high-power-density redox
638 flow batteries. *ACS Energy Lett*., 2023, **8**, 3526-3535.
639 50. L. Tang, P. Leung, Q. Xu, M. R. Mohamed, S. Dai, X. Zhu, C. Flox and A. A. Shah, Future
640 perspective on redox flow batteries: aqueous versus nonaqueous electrolytes. *Curr. Opin. Chem.*
641 *Eng.*, 2022, **37**, 100833.

View Article Online
DOI: 10.1039/D6TA01059H

642 51. J. Xie, S. Sankarasubramanian and V. Ramani, Asymmetric electrode configurations enhance
643 operating power density and energy efficiency of an aqueous, electrode-decoupled titanium–
644 cerium redox flow battery. *Sustain. Energy Fuels*, 2026, **10**, 1147-1164.
645 52. S. Sankarasubramanian and V. Ramani, Redox flow battery, *US Pat*., 11177497, 2021.
646 53. Z. Wang, S. Sankarasubramanian, V. Ramani, Y. Zhang and J. Parrondo, Doped anion
647 exchange membranes (AEMs) for highly selective separators in electrochemical devices *US Pat*.,
648 12521758, 2026.
649 54. S. Sankarasubramanian, Y. Zhang, C. He, T. Gregory and V. Ramani, An Aqueous, Electrode-
650 Decoupled Redox-Flow Battery for Long Duration Energy Storage, preprint, 2021, DOI:
651 10.21203/rs.3.rs-150474/v1.
652 55. J.-M. Savéant and D. Tessier, Potential dependence of the electrochemical transfer coefficient.
653 Reduction of some nitro compounds in aprotic media, *J. Phys. Chem*., 1977, **81**, 2192–2197.
654 56. M. T. Lawder, B. Suthar, P. W. C. Northrop, S. De, C. M. Hoff, O. Leitermann, M. L. Crow,
655 S. Santhanagopalan and V. R. Subramanian, Battery Energy Storage System (BESS) and Battery
656 Management System (BMS) for Grid-Scale Applications. *Proc. IEEE*, 2014, **102**, 1014-1030.
657 57. V. Scaini, P. J. Lex, T. W. Rhea and N. H. Clark, Battery energy storage for grid support
658 applications. https://www.sandia.gov/ess-ssl/EESAT/2002_papers/00002.pdf
659 58. Y. Cao, S. B. Lee, V. R. Subramanian and V. M. Zavala, Multiscale model predictive control
660 of battery systems for frequency regulation markets using physics-based models. *J. Process*
661 *Control*, 2020, **90**, 46-55.
662 59. C. L. Nge, I. U. Ranaweera, O.-M. Midtgård and L. Norum, A real-time energy management
663 system for smart grid integrated photovoltaic generation with battery storage. *Renew. Energy*, 2019,
664 **130**, 774-785.
665 60. X. Gao, D. Zhou, A. Anvari-Moghaddam and F. Blaabjerg, A Comparative Study of Grid-
666 Following and Grid-Forming Control Schemes in Power Electronic-Based Power Systems. *PEAD*.,
667 2023, **8**, 1-20.
668

View Article Online
DOI: 10.1039/D6TA01059H

References cited in the Supplementary Information (SI)

1. S. A. Hayes, P. Yu, T. J. O'Keefe, M. J. O'Keefe and J. O. Stoffer, The phase stability of cerium species in aqueous systems: I. E-pH diagram for the system. *J. Electrochem. Soc*., 2002, **149**, C623-C630.
2. B. Bouchaud, J. Balmain, G. Bonnet and F. Pedraza, pH-distribution of cerium species in aqueous systems. *J. Rare Earths*, 2012, **30**, 559-562.
3. Q. Sun, The Raman OH stretching bands of liquid water. *Vib. Spectrosc*., 2009, **51**, 213-217.
4. C. A. Buchanan, D. Herrera, M. Balasubramanian, B. R. Goldsmith and N. Singh, Unveiling the cerium(III)/(IV) structures and charge-transfer mechanism in sulfuric acid. *JACS Au*, 2022, **2**, 2742-2757.

View Article Online
DOI: 10.1039/D6TA01059H

Data Availability Statement

All of the data associated with these studies are represented in the manuscript and supplemental information. The raw data are available from the corresponding author upon reasonable request. The references cited in the Supplementary Information (SI) have been listed at the bottom of the reference section in the manuscript.